International Journal of Nanomedicine

Dovepress
open access to scientific and medical research

Open Access Full Text Article

ORIGINAL RESEARCH

# $Fe_3O_4$ Nanoparticles That Modulate the Polarisation of Tumor-Associated Macrophages Synergize with Photothermal Therapy and Immunotherapy (PD-1/PD-L1 Inhibitors) to Enhance Anti-Tumor Therapy

Haishui Sun[1,*], Xiao Wang[2,3,*], Zhaoyang Guo[4,*], Zhenrong Hu[5], Yuanchen Yin[4], Shuhan Duan[6], Wenwen Jia[2], Wei Lu[2,3], Jingzhou Hu[1,7]

[1]Department of Oral and Maxillofacial - Head and Neck Oncology, Shanghai Ninth People's Hospital, Shanghai Jiao Tong University School of Medicine; College of Stomatology, Shanghai Jiao Tong University; National Center for Stomatology; National Clinical Research Center for Oral Diseases; Shanghai Key Laboratory of Stomatology & Shanghai Research Institute of Stomatology, Shanghai, People's Republic of China; [2]Institute for Regenerative Medicine, Shanghai East Hospital, School of Life Sciences and Technology, Tongji University, Shanghai, People's Republic of China; [3]Shanghai Key Laboratory of D&A for Metal Functional Materials, School of Materials Science and Engineering, Tongji University, Shanghai, People's Republic of China; [4]School of Stomatology, Weifang Medical University, Weifang, Shandong Province, People's Republic of China; [5]Department of Stomatology, Shanghai East Hospital, School of Medicine, Tongji University, Shanghai, People's Republic of China; [6]Shanghai Key Laboratory of Stomatology, Department of Oral Surgery, Shanghai Ninth People's Hospital, College of Stomatology, National Center for Stomatology, National Clinical Research Center for Oral Diseases, Shanghai Research Institute of Stomatology, Shanghai Jiao Tong University School of Medicine, Shanghai Jiao Tong University, Shanghai, People's Republic of China; [7]Department of Oral and Maxillofacial Surgery, Zhang Zhiyuan Academician Workstation, Hainan Western Central Hospital, Shanghai Ninth People's Hospital, Danzhou, Hainan, People's Republic of China

*These authors contributed equally to this work

Correspondence: Jingzhou Hu; Wei Lu, Email huyayi@shsmu.edu.cn; weilu@tongji.edu.cn



**Introduction:** Traditional surgical resection, radiotherapy, and chemotherapy have been the treatment options for patients with head and neck squamous cell carcinoma (HNSCC) over the past few decades. Nevertheless, the five-year survival rate for patients has remained essentially unchanged, and research into treatments has been relatively stagnant. The combined application of photothermal therapy (PTT) and immunotherapy for treating HNSCC has considerable potential.

**Methods:** Live-dead cell staining and CCK-8 assays proved that $Fe_3O_4$ nanoparticles are biocompatible in vitro. In vitro, cellular experiments utilized flow cytometry and immunofluorescence staining to verify the effect of $Fe_3O_4$ nanoparticles on the polarisation of tumor-associated macrophages. In vivo, animal experiments were conducted to assess the inhibitory effect of $Fe_3O_4$ nanoparticles on tumor proliferation under the photothermal effect in conjunction with BMS-1. Tumour tissue sections were stained to observe the effects of apoptosis and the inhibition of tumor cell proliferation. The histological damage to animal organs was analyzed by hematoxylin and eosin (H&E) staining.

**Results:** The stable photothermal properties of $Fe_3O_4$ nanoparticles were validated by in vitro cellular and in vivo animal experiments. $Fe_3O_4$ photothermal action not only directly triggered immunogenic cell death (ICD) and enhanced the immunogenicity of the tumor microenvironment but also regulated the expression of tumor-associated macrophages (TAMs), up-regulating CD86 and down-regulating CD206 to inhibit tumor growth. The PD-1/PD-L1 inhibitor promoted tumor suppression, and reduced tumor recurrence and metastasis. In vivo studies demonstrated that the photothermal action exhibited a synergistic effect when combined with immunotherapy, resulting in significant suppression of primary tumors and an extension of survival.

**Conclusion:** In this study, we applied $Fe_3O_4$ photothermolysis in a biomedical context, combining photothermolysis with immunotherapy, exploring a novel pathway for treating HNSCC and providing a new strategy for effectively treating HNSCC.

**Keywords:** photothermal therapy, immunotherapy, tumor-associated macrophages, head and neck squamous cell carcinoma



Received: 20 February 2024
Accepted: 22 June 2024
Published: 17 July 2024

## Introduction

Head and neck squamous cell carcinoma (HNSCC) is the sixth most common cancer worldwide, with more than 6,000,000 patients diagnosed each year.[1–3] In recent decades, human beings have never stopped exploring treatment modalities for HNSCC, but the five-year survival rate of patients with head and neck squamous cell carcinoma has barely improved.[4,5] Conventional means of treating squamous cell carcinoma of the head and neck include surgical resection, chemotherapeutic drugs, radiotherapy, and immunotherapy. However, surgical resection often results in the loss of tissues or organs, and chemotherapeutic drug treatment kills normal cells while killing tumor cells.[2,6,7] Therefore, a more in-depth exploration of therapies for HNSCC has far-reaching implications.

Photothermal therapy (PTT) effectively converts light energy into heat and thus inhibits tumor growth. Photothermal agents produce heat when they are exposed to near-infrared light. The PTT method is based on the idea that this heat can be used for therapeutic purposes.[8] It has gained the attention of more and more scholars due to its low trauma, extremely low toxicity and side effects, and highly effective physical tumor-killing product.[9–11] Because of their exceptional biocompatibility, iron oxide nanoparticles ($Fe_3O_4$) have garnered significant interest as a photothermal converter for creating diverse therapeutic nanoplatforms. $Fe_3O_4$ has been utilized as a highly effective photothermal conversion substance in tumor ablation therapy.[12–14]

One of the most promising modalities for tumor immunotherapy is the ability of photothermal action to trigger immunogenic cell death (ICD).[15–18] It has been demonstrated that elevated temperatures under photothermal action can lead to apoptosis of tumor cells. The principal reasons for this phenomenon are cell membrane damage, intracellular protein denaturation, and RNA/DNA synthesis disruption in tumor cells caused by elevated temperatures.[19,20] Mocan et al demonstrated that photothermal effects can depolarize the mitochondrial membrane, leading to cellular damage.[21] Phenylalanine metabolism is also disrupted by PTT, as are the activities of specific apoptotic proteins, which in turn promote apoptosis.[22]

Furthermore, the expression of heat shock proteins is also associated with photothermal-induced cell death mechanisms.[23] It has been demonstrated that inhibiting the expression of a variety of heat shock proteins (HSPs), including HSP70, reduces the heat resistance of tumor cells, enhancing the sensitivity of tumors to PTT and improving the efficiency of PTT.[19,24,25] Photothermal action directly induces immunogenic cell death (ICD) of tumor cells while simultaneously releasing tumor-associated antigens and damage-associated molecular patterns (DAMP) to stimulate immune responses and enhance the immunogenicity of the tumor microenvironment.[26–32] Research has demonstrated that an increased release of DAMPs, including different types of heat shock proteins, occurs within the temperature range of 39–45°C.[33,34] This heightened release can enhance immunostimulatory effects, with mild heating between 42–45°C conducive to creating an immune-responsive tumor microenvironment (TME).[11,35] However, the inability of PTT to kill tumors outside the range of light should not be overlooked, and a single treatment modality is usually not enough to completely cure a cancer.[36,37] More and more researchers are focusing on combining photothermal action with other therapeutic modalities.

Immunotherapy has significant advantages due to its systemic modulatory capacity, which reduces immunoregulatory suppression and recurrence and metastasis rates. On the one hand, immunotherapy increases the immunogenicity of the tumor microenvironment (using immune adjuvants) and recruits more dendritic cells (DCs). On the other hand, it can reduce immunomodulatory suppression, thus increasing tumor-infiltrating cytotoxic CD8+ T cells and effector memory T cells.[38] In immunotherapy, PD-1/PD-L1 checkpoint blockade is one of the most widely used strategies in cancer immunotherapy.[39] PD-1/PD-L1 inhibitors specifically bind to tumor cells or T-cell receptors, promoting T-cell-mediated recognition and immune function.[40] HNSCC has identified the PD-1 pathway as a valid target.[41,42] Although immunotherapy can induce systemic anti-tumor immunity, it is relatively ineffective in removing solid primary tumors.[43]

PTT alone may not be effective for distal and residual tumors, but it can complement its effects when combined with immunotherapy. While immunotherapy may have limitations for solid tumors, PTT can directly kill cancer cells effectively, making the combination of PTT and immunotherapy a promising approach.[44] This study investigated an unconventional treatment for HNSCC by combining the photothermal action of $Fe_3O_4$ nanoparticles with immunosuppressive therapy. In vivo and ex vivo experiments confirmed that the photothermal action could promote the body's immune response while killing the tumor cells. When combined with PD-1/PD-L1 immunosuppression, the noticeable tumor suppression effect was

evident in the in vivo animal model, which improved the survival rate of the experimental animals. Combining the systemic effects of immunotherapy with the ease of making $Fe_3O_4$ nanoparticles and their low toxicity and side effects, they can not only play to their strengths but also make up for each other's weaknesses, creating synergistic therapeutic effects and a very effective strategy that has much potential for targeting and treating clinical HNSCC.

# Experiment

## Materials

Specific reagents and material sources are listed below: $FeCl_3 \cdot 6H_2O$ (Aladdin, Shanghai, China), Dulbecco's Modified Eagle Medium (HyClone, USA), 96-well and 6-well plates (Corning, New York, USA), Confocal dish(Beyotime, Shanghai, China), phosphate buffer saline (Gibco, Carlsbad, CA, USA), Penicillin/streptomycin (Gibco, USA), CCK-8 kit instructions (DOJINDO, Kumamoto, Japan), live-dead cell staining kit (Beyotime, Shanghai, China), DAPI (Solarbio, Beijing, China), Trizol(Invitrogen), Fetal bovine serum (Gibco, Australia), IL-4 ELISA Kit (Jonln, Shanghai, China), TNF-α ELISA Kit (Neobioscience, Shenzhen, China), BMS-1(PD-1/PD-L1 inhibitor 1, Selleck, USA), Shimadzu UV-3600i Plus, Microscope (TE2000-U, Nikon, Tokyo, Japan).

## Preparation of $Fe_3O_4$ Nanodisc

The $Fe_2O_3$ nanodiscs were synthesized chemically. α-$Fe_2O_3$ nanodiscs were prepared by a simple alcohol-thermal reaction in which a certain amount of $FeCl_3 \cdot 6H_2O$, distilled water, sodium acetate ($CH_3COONa$), and ethanol were mixed by magnetic stirring in a typical synthesis. The mixture was then sealed in a stainless-steel autoclave with a Teflon liner and held at 180°C for 12 hours. After cooling to room temperature, the red product was collected by centrifugation and washed with distilled water. The $Fe_3O_4$ nanodiscs were achieved by thermal annealing at 500°C under a hydrogen/argon (95% Ar+5% $H_2$) atmosphere for 1 hour. The $Fe_3O_4$ nanodiscs were stored in a dry and light-protected environment. They can be prepared whenever needed for Experiments.

## Physical Characterization of $Fe_3O_4$

This study used a DX-2700 X-ray diffractometer (Cu-Kα radiation, λ = 1.54 Å) to obtain the X-ray diffraction (XRD) patterns. Transmission electron microscopy (TEM) techniques are utilized to examine a sample's original shape and structure, providing detailed data like thickness and diameter. A Shimadzu UV-3600i Plus was used to measure the UV-Vis-NIR absorption spectra of $Fe_3O_4$. The heating curve of $Fe_3O_4$ at 808 nm NIR light brother was observed using FOTRIC 285s. The images were plotted using Origin 2019.

## Cell Acquisition and Culture conditions

We obtained RAW264.7 and SCC7 cells from Shanghai Jiao Tong University School of Medicine's Ninth People's Hospital. The cell culture medium was standard:[4] 90% DMEM + 10% FBS + 1% P/S. Every three days, we passed RAW264.7 cells and SCC7 cells. Cell incubator environment: 95% air + 5% carbon dioxide, constant 37 °C. For future experiments, we used cells in a satisfactory state.

## $Fe_3O_4$ Nanoparticle Concentration Settings

Based on previous research,[45] $Fe_3O_4$ nanoparticles were set in 5 concentration groups of 2 mg/mL, 1 mg/mL, 0.5 mg/mL, 0.25 mg/mL, and 0.1 mg/mL. An appropriate amount of $Fe_3O_4$ photothermal nanoparticles was weighed, and the complete medium was added to mix $Fe_3O_4$ photothermal nanoparticles and configured into the desired concentration. The control group did not include $Fe_3O_4$ nanoparticles.

## CCK-8 and Live/Dead Staining Assays

The CCK-8 assay verified the biosafety of $Fe_3O_4$ suspensions at different concentrations against RAW264.7 and SCC7 cells. RAW264.7 and SCC7 cell lines were seeded in 96-well plates at densities of $5\times10^3$ cells per well and $3\times10^3$ cells per well, respectively. After cell adhesion, we maintained the cultures for 1 and 3 days using varying concentrations of

the $Fe_3O_4$ mixture. Upon reaching the time point, we conducted the experiments following the CCK-8 kit instructions, subsequently reading and analyzing the data under the OD450 condition of the enzyme marker.

$Fe_3O_4$ in vitro cell biosafety was further verified by live/dead cell staining. RAW264.7 and SCC7 cell lines were seeded in 96-well plates at densities of $5\times10^3$ cells per well and $3\times10^3$ cells per well, respectively. Following a 6-hour incubation period for cell adhesion, introduce the $Fe_3O_4$ mixture and proceed to incubate the cells for an additional 24 hours in a dark environment. The $Fe_3O_4$ suspension was washed with PBS buffer, stained in compliance with the live-dead cell staining kit, and photographed under the fluorescence microscope(Olympus Corporation, Tokyo, Japan).

## Promotion of SCC7 Cell Killing by $Fe_3O_4$ by Photothermal Effects

The killing effect of 2 mg/mL $Fe_3O_4$ on SCC7 cells under NIR light irradiation was analyzed by live-dead cell staining. Inoculate SCC7 cells at a density of $2\times10^5$ cells per well in a 6-well plate and allow for a 6-hour incubation period to facilitate cell adhesion to the culture plate. Next, we introduced a suspension containing $Fe_3O_4$ at a 2 mg/mL concentration and immediately exposed the cells to NIR light. We used groups without $Fe_3O_4$ nanoparticles and NIR irradiation as blank controls and groups with only $Fe_3O_4$ nanoparticles without NIR irradiation as negative controls. The light conditions were 808 nm near infrared light (1 W/cm$^2$, 5 min). After 4 hours of continued incubation, live/dead cell staining was performed, and photographs were taken to observe the survival of SSC7 cells. To analyze the killing effect of $Fe_3O_4$ photothermal action on SCC7 cells.

## Preparation of Conditioned Media

Inoculate SCC7 cells at a density of $2\times10^5$ cells per well in a 6-well plate and allow for a 6-hour incubation period to facilitate cell adhesion to the culture plate. Next, we introduced a medium containing 2 mg/mL of $Fe_3O_4$ and then exposed the cells to 808 nm near-infrared (NIR) light for 5 minutes (1W/cm$^2$). The control group did not include any $Fe_3O_4$ nanoparticles and NIR exposure. Both experimental groups included $Fe_3O_4$ nanoparticles, with the distinction that one group was subjected to NIR light irradiation while the other was not. After incubation, we aspirated the cell supernatant into an aseptic centrifuge tube and centrifuged it for 10 minutes at 1500 rpm. The supernatant was then filtered using a 0.22 μm filter. The conditioned medium is the filtered supernatant of cell groups combined with twice the volume of cell culture medium. We thoroughly mix this mixture and store it in a refrigerator set to −20°C as a reserve.

## Macrophage Immunofluorescence Assay

Introduce $1\times10^5$ RAW264.7 cells into each confocal dish (20mm) and allow them to incubate for 6 hours. After the cells were adhered to the wall, 1 mL of conditioned medium was added, and the culture was continued for 24 hours. The medium was aspirated, fixed in 4% paraformaldehyde for 30 minutes, washed with PBS and sequentially subjected to 0.5% Triton X-100 permeabilization, 5% BSA blocking, incubated with rabbit CD86 and CD206 primary antibodies overnight at 4°C and incubated with donkey anti-rabbit secondary antibodies before DAPI nuclear staining and observation and photography by fluorescence microscopy(TE2000-U, Nikon, Tokyo, Japan).

## Q-PCR to Detect Tumor-Associated Macrophage Gene Expression

The RAW264.7 cells were seeded in 6-well plates at a density of $5\times10^5$ cells/well. Following a 6-hour incubation period for cell adhesion, 2 mL of conditioned medium was introduced into each well. The cells were then cultured for a period of 24 hours. We used the Trizol method to extract RNA and the reverse transcription reagent to obtain cDNA. The cDNA was amplified using a Roche PCR instrument, the ct value data were obtained, and the data were analyzed following the formula $2^{-\Delta\Delta Ct}$ data analysis. The primer sequences of the relevant genes are shown in Table 1.

## Elisa Assay to Detect Cytokine Secretion

The RAW264.7 cells were seeded in 6-well plates at a density of $5\times10^5$ cells/well. Following a 6-hour incubation period for cell adhesion, 2 mL of conditioned medium was introduced into each well. We then cultured the cells for 24 hours. Aspirate the supernatant of each group and follow the instructions of Elisa kit to detect the content of TNF-α and IL-4 in the cell supernatant respectively.

**Table 1** Related Primer Sequences

| Gene | Forward Primer (5'–3') | Reverse Primer (5'–3') |
|---|---|---|
| CD86 | TGTTTCCGTGGAGACGCAAG | TTGAGCCTTTGTAAATGGGCA |
| IL-6 | CTTCTTGGGACTGATGCTGGTGAC | AGGTCTGTTGGGAGTGGTATCCTC |
| IL-1β | TCGCAGCAGCACATCAACAAGAG | AGGTCCACGGGAAAGACACAGG |
| CD206 | CTCTGTTCAGCTATTGGACGC | CGGAATTTCTGGGATTCAGCTTC |
| Arg-1 | GGCAACCTGTGTCCTTTCTCCTG | GGTCTACGTCTCGCAAGCCAATG |
| IL-4 | GGTCTCAACCCCCAGCTAGT | GCCGATGATCTCTCTCAAGTGAT |
| IL-10 | GCTCTTACTGACTGGCATGAG | CGCAGCTCTAGGAGCATGTG |
| TNF-α | GCCTCTTCTCATTCCTGCTTGTGG | GTGGTTTGTGAGTGTGAGGGTCTG |
| GAPDH | ACCCAGAAGACTGTGGATGG | CACATTGGGGGTAGGAACAC |

## Flow Cytometry

The RAW264.7 cells were seeded in 6-well plates at a density of $5\times10^5$ cells/well. Following a 6-hour incubation period for cell adhesion, 2 mL of conditioned medium was introduced into each well. The cells were then cultured for a period of 24 hours. We collected cells, tested them on the machine, and obtained data, including the ratio of CD206 to CD86 in RAW264.7 cells, which were analyzed.

## In vivo Animal Experiments

Subcutaneous implantation of SCC7 is a well-established animal model of HNSCC for preclinical studies.[1,4,46] The Animal Center of the Ninth People's Hospital, affiliated with Shanghai Jiaotong University School of Medicine, provided the experimental rats used in this experiment and approved the experimental procedures involving animals (SH9H-2023-A792-1). The animal experimental operations were conducted following the provisions of the Animal Welfare Law. Twenty female C3H/HeN mice of 4 weeks of age were purchased and fed for 1–2 weeks to allow them to acclimate to the environment. Cells were prepared before the experiment, and SCC7 was resuspended in sterile PBS at a concentration of $1\times10^7$/mL and kept on ice. After the right side of the mouse skin was shaved and sterilized with alcohol, 100 μL of SCC7 cell suspension was injected subcutaneously. BMS-1 is used as a small molecule compound inhibitor of PD-1/PD-L1 interaction.[47] After tumor implantation for 7 days, the mice were randomly divided into 4 groups: control group, NIR group, BMS-1 group and NIR+BMS-1 group. The NIR group received subcutaneous injections of $Fe_3O_4$ photothermal material every 2 days and underwent NIR light irradiation (1 W/cm$^2$, 5 min). The BMS-1 group received intraperitoneal injections of 100 μL of the PD1/PD-L1 inhibitor BMS-1 every 2 days. The NIR+BMS-1 group received both NIR irradiation and intraperitoneal injections of BMS-1. The control group received intraperitoneal injections of 100 μL sterile PBS every 2 days. Tumors were measured with calipers every 2 days and mice were sacrificed when tumors were necrotic or exceeded 2000 mm$^3$. (Tumor volume calculation formula: 1/2 × width$^2$ × length).

## Histopathological Analysis

After a certain period, C3H/HeN mice were decapitated and executed, and their major organs (kidney, spleen, heart, liver, lung) and tumor tissues were dissected and isolated. The collected tumors and other tissues were immersed in 4% paraformaldehyde for fixation. Upon completion of fixation, paraffin-embedded sections and tumor tissue staining was performed, and morphological changes in each group were observed under a microscope(TE2000-U, Nikon, Tokyo, Japan) and photographed for documentation. Tumor tissue immunofluorescence staining was quantified using the Image J software.

## Statistical Analyses

All graphical statistical analyses in the experiment were performed using GraphPad Prism 8 software. In this case, the data were expressed as mean ± standard deviation (SD), the difference between the groups was analyzed and compared using a *t*-test, the differences between the three groups were analyzed using one-way ANOVA, and a 95% confidence interval was chosen as the significance of the differences between the groups. $p<0.05$ was considered statistically

significant, " # " indicates that the experimental group was statistically significant compared with the control group, $^{\#}p<0.05$,$^{\#\#}p<0.01$. " * " means that the comparison between the two groups is statistically significant, *p<0.05,**p<0.01.

## Results and Discussion

### Characterizations of $Fe_3O_4$

As shown in Figure 1a and b and Supplementary Figure 1, the thickness (T) of $Fe_3O_4$ is about 26 nm, the average diameter (D) is approximately 225 nm, the aspect ratio (D/T) is about 8.6, and the particle has significant shape anisotropy. It has been demonstrated that $Fe_3O_4$ nanoparticles with 60–200 nm diameters can effortlessly exude from microvessels and penetrate deep into the tumor stroma. Simultaneously, it was observed that larger $Fe_3O_4$ nanoparticles displayed enhanced retention and aggregation within the tumor in comparison to smaller nanoparticles.[48] This phenomenon can be ascribed to the increased velocity of smaller nanoparticles within blood vessels, leading to a higher probability of exiting the tumor than their larger counterparts.[48,49] The X-ray diffraction patterns of the $Fe_3O_4$ samples gave sharp XRD peaks as shown in Figure 1c, and all the prominent peaks (220), (311), (400), (422), (511) and (440) were observed at the corresponding angles in the peak positions. Consistent with previous studies.[45] As shown in Figure 1d, the UV-Vis-NIR absorption spectra of $Fe_3O_4$ NDs, a narrow absorption band from 400 nm to 1100 nm, were observed, revealing the NIR photothermal capability of $Fe_3O_4$. The temperature changes of $Fe_3O_4$ solutions with different concentrations when exposed to an 808 nm laser for 5 minutes are depicted in Figure 1e. Significantly, an outstanding photothermal performance was observed with a concentration of 2 mg/mL of Fe3O4, resulting in a maximum temperature differential of approximately 40°C. The $Fe_3O_4$ nanodiamonds also exhibited favorable near-infrared (NIR) photothermal stability, as illustrated in Figure 1f.

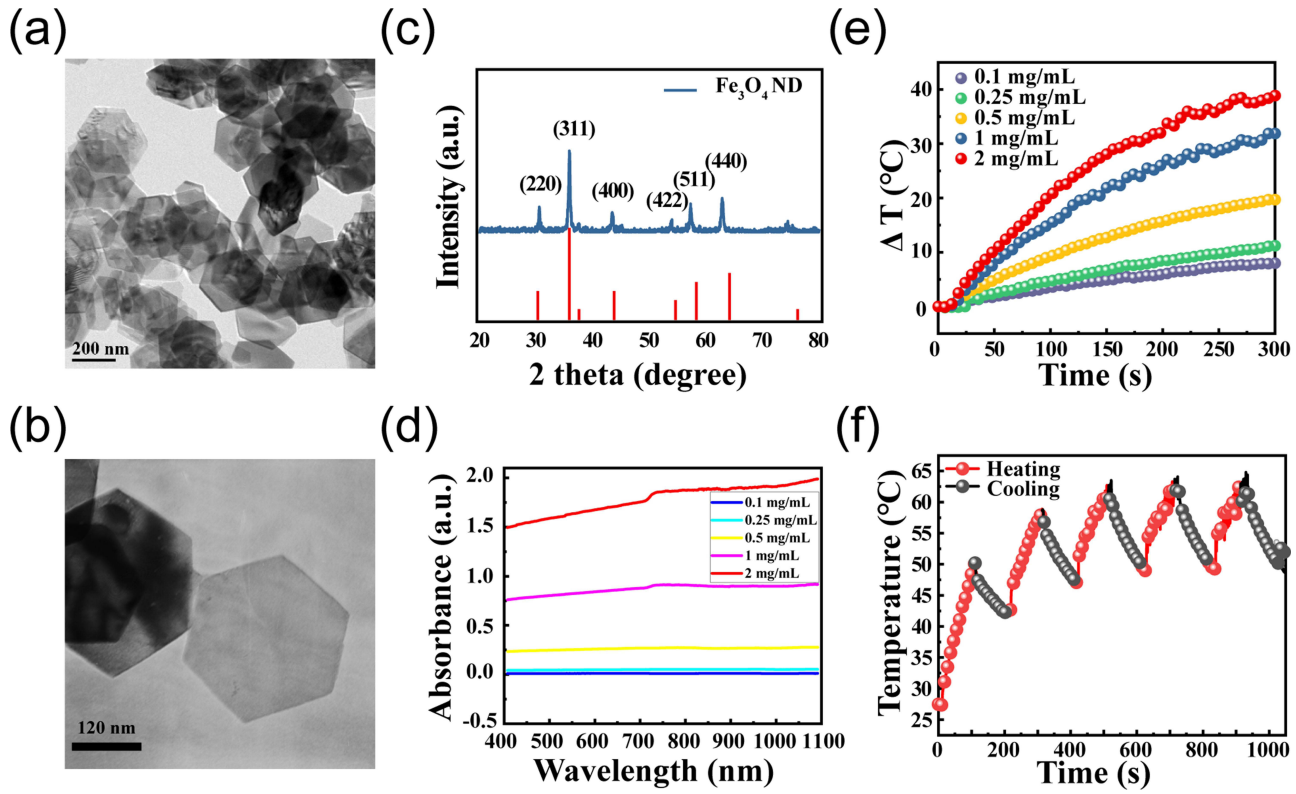


**Figure 1** (**a**) and (**b**) Depict TEM images showcasing the synthesized NDs after reduction. (**c**)X-ray diffraction pattern of $Fe_3O_4$. (**d**)UV−vis−NIR absorption spectra and of $Fe_3O_4$ solutions at different concentrations. (**e**)Temperature elevating curves of $Fe_3O_4$ at various concentrations under NIR laser irradiation for 5 min (808 nm, 1 W/cm$^2$). (**f**)The photothermal stability of $Fe_3O_4$ under laser irradiation (5 cycles, 808 nm, 1 W/cm$^2$).

## Biocompatibility of $Fe_3O_4$

The biocompatibility of iron tetraoxide nanoparticles was validated using a CCK-8 analysis on RAW264.7 cells (Figure 2a) and SCC7 cells (Figure 2b). As shown in Figure 2a, RAW264.7 cells were cultured in different concentrations of $Fe_3O_4$ medium for 1 day, with no statistical difference between groups; continuing the culture to day 3, 0.5 mg/mL, 1 mg/mL and 2 mg/mL were lower than the OD values of the control group, and 1 mg/mL and 2 mg/mL were lower than those of the 0.1 mg/mL group, which was considered to be because RAW264.7 cells adhered to the wall. In the late proliferation stage, the high concentration of $Fe_3O_4$ nanoparticles occupies a larger area than the low concentration of $Fe_3O_4$ nanoparticles. This limits the proliferation space of RAW264.7 cells in the late proliferation stage. The biocompatibility of different concentrations of $Fe_3O_4$ with RAW264.7 was verified by the live and dead cell staining experiments in Figure 2a and c. After incubating RAW264.7 cells with various concentrations of $Fe_3O_4$ for 24 hours, a significant number of viable cells (green) and a minor number of nonviable cells (red) were observed in all experimental groups. There was no significant difference in the groups compared to the control group. In a previous study, $Fe_3O_4$ medium at 2 mg/mL did not produce substantial toxicity to CAL27 cells.[45] It has been shown that $Fe_3O_4$ nanoparticles at a concentration of 0–2 mg/mL have no toxic effects on cells in vitro or in vivo in the absence of NIR laser irradiation. There was no significant organ damage during treatment with NIR laser irradiation of injected nanoparticles.[48] The outcomes of the live-dead cell staining analysis in this investigation were consistent with the results derived from the CCK-8 assay, thereby confirming the biocompatibility demonstrated by $Fe_3O_4$ at a dosage of 2 mg/mL when evaluated on RAW264.7 cells.

As depicted in Figure 2b, on the first day of the experiment, a concentration of 0.1 mg/mL of $Fe_3O_4$ exhibited notable toxicity compared to the control medium lacking $Fe_3O_4$. In contrast, 2 mg/mL of $Fe_3O_4$ concentration demonstrated an even more pronounced toxic impact. On day 3, the same trend observed on day 1 continued. We confirmed the poisonous influence of $Fe_3O_4$ on SCC7 cells, and the harmful effect strengthened with the increase in concentration. The detrimental impact of $Fe_3O_4$ on SCC7 cells was more clearly observed by staining both live and

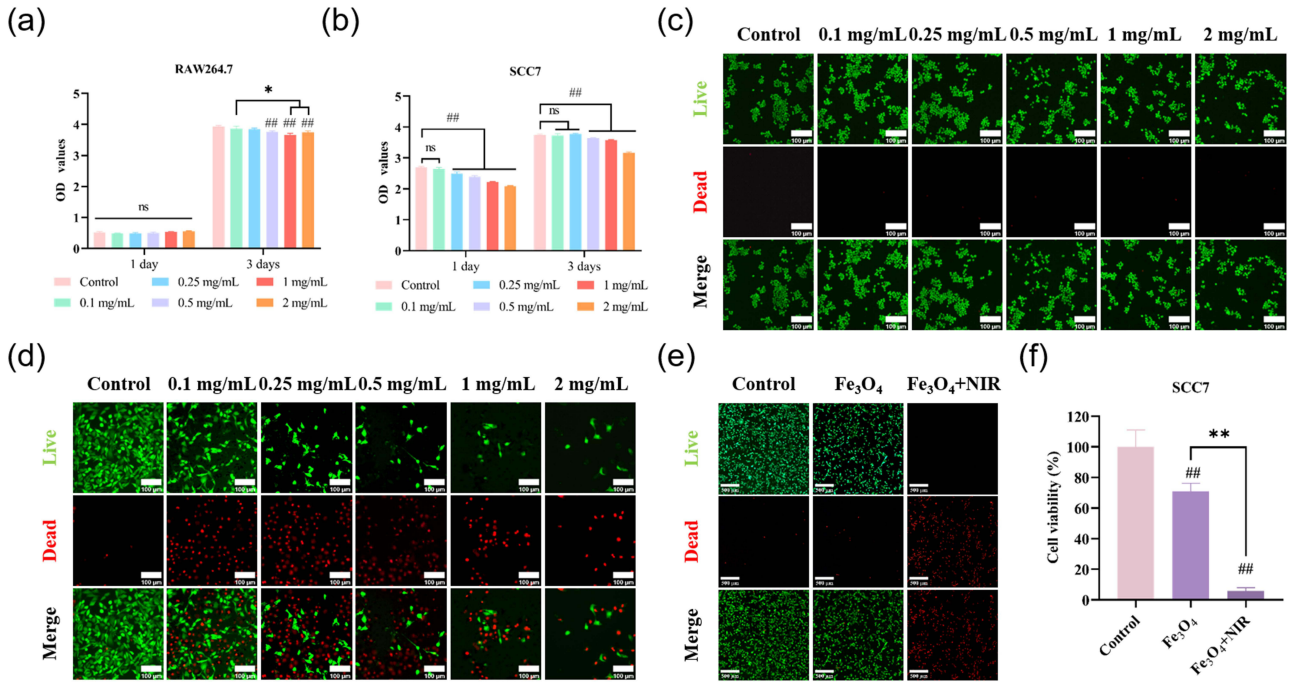


**Figure 2** Biocompatibility and photothermal cell killing of $Fe_3O_4$ in vitro. (**a** and **b**) are CCK-8 analyses of RAW264.7 cells and SCC7 cells cultured in different concentrations of $Fe_3O_4$ medium for 1 day and 3 days. (**c** and **d**) are live-dead cell staining of RAW264.7 cells and SCC7 cells cultured with different concentrations of $Fe_3O_4$ for 1 day. (**e**) Live-dead cell staining of SCC7 cells after 2 mg/mL $Fe_3O_4$ photothermolysis followed by incubation for 4 hours. (**f**) Survival analysis of SCC7 cells after 2 mg/mL $Fe_3O_4$ photothermal action and continued incubation for 4 hours. "#" indicates that the experimental group was statistically significant compared with the control group, $^{\#\#}p<0.01$. "*" means that the comparison between the two groups is statistically significant, $^{*}p<0.05$,$^{**}p<0.01$. The scale bar indicates 100 μm.

dead cells. Figure 2d illustrates that after culturing SCC7 cells with various $Fe_3O_4$ concentrations for 24 hours, the 2 mg/mL Fe3O4 group showed only a tiny number of surviving SCC7 cells compared to the blank control. The live-dead cell staining results were consistent with the general trend of the CCK-8 experimental results. 2 mg/mL $Fe_3O_4$ had a toxic effect on SCC7 cells.

The potential toxicity of photothermal agents is the most critical issue in photothermal action.[50,51] Non-degradable or slowly degrading nanoparticles quickly accumulate in body organs, leading to oxidative stress, inflammatory cytokine production and cell death.[52] As a nutrient, iron is metabolized rapidly by cellular regulation using the transferrin pathway. Meanwhile, $Fe_3O_4$ nanoparticles are easily degraded. They can cross the plasma membrane to enter and exit cells.[50] $Fe_3O_4$ nanoparticles are well suited for in vivo applications due to their advantages. This study used 2 mg/mL $Fe_3O_4$ without significant toxicity to RAW264.7 cells, consistent with previous studies. However, 2 mg/mL $Fe_3O_4$ has specific toxicity to SCC7 cells. From the perspective of killing tumor cells, it can kill tumor cells directly and SCC7 cells through PTT, which undoubtedly achieves the effect of "double promotion".

## Tumor Killing by Photothermal Action of $Fe_3O_4$

As can be seen in Figure 2e, a large number of dead cells and a small number of live cells were found in the photothermal group compared with the control group and $Fe_3O_4$ group, confirming that $Fe_3O_4$ photothermal action can kill a large number of tumor cells in a short period. The in vitro tumor cell-killing effect was further verified by CCK-8 experiments, as shown in Figure 2f. The photothermal action on SCC7 cells was continued for 4 hours, and the survival rate of SCC7 cells in the $Fe_3O_4$ group alone was 71.06±4.67%, while it was only 5.78±1.90% in the photothermal group. The photothermal group significantly reduced the survival rate of SCC7 cells and appeared to kill tumor cells. Live and dead cell staining and CCK-8 tests showed that the 2 mg/mL $Fe_3O_4$ photothermal result effectively killed the tumors.

## Tumor-Associated Macrophages in vitro

The expression of tumor-associated macrophage genes was detected using Q-PCR (Figure 3a) and flow cytometry (Figure 3b). CD86 is a typical phenotype of M1-type macrophages. As shown in Figure 3a, both the control group and the $Fe_3O_4$ alone group showed low expression of CD86. On the other hand, the photothermal group had a lot of the CD86 protein, which was in line with the immunofluorescence CD86 protein expression trend shown in Figure 3c. This was also true for TNF-α, IL-6, and IL-1β, all M1-type macrophage-associated factors. The related mRNA expression was consistent with CD86 expression, and the photothermal group showed the highest expression among all groups. CD206 is a typical phenotype of M2 macrophages.[53] The CD206 gene expression level was going opposite to CD86, as shown in Figure 3a. The CD206 gene expression level was lower in the photothermal group compared to the blank control group and the $Fe_3O_4$ alone group. This was in line with the immunofluorescence CD206 protein expression trend shown in Figure 3d. The mRNA expression of Arg-1, IL-4, and IL-10, which are factors associated with M2-type macrophages, was consistent with that of CD206; in all groups, the photothermal group exhibited low expression. Flow cytometry further confirmed the polarization of RAW264.7 cells. The photothermal group had the lowest percentage of CD206 cells (3.62%) and the highest rate of CD86 cells (0.23%), as shown in Figure 3b. This was in line with the results of immunofluorescence staining and q-PCR. The RAW264.7 cells in the photothermal group showed a more heightened M1 polarisation and lower M2 polarisation than the rest. In the Elisa assay, the experiment was used to detect the expression shown in Figure 3e and f and determine how many factors were present in the cell supernatant. The group exposed to light had the highest levels of TNF-α and the lowest levels of IL-4. The expression trends of TNF-α and IL-4 are shown in Figure 3a.

In tumor tissues, tumor-associated macrophages consist of two main subpopulations, with M1-like macrophages being potent effector cells that kill tumor cells. TAMs predominantly display an M1 phenotype with anti-tumor properties in the early stages of tumor progression.[54] The M1 type has a high antigen-presenting capacity, promotes the proliferation of CD8+ T cells and NK cells via IL-6 and TNF-α, enhances cytotoxicity to induce tumor cell apoptosis, and improves immune stimulation.[55–57] M2-like macrophages can speed up the growth and metastasis of tumors in some ways, and TAMs inside or close to tumors often show M2-type characteristics.[58] CD206 can promote the proliferation and invasion

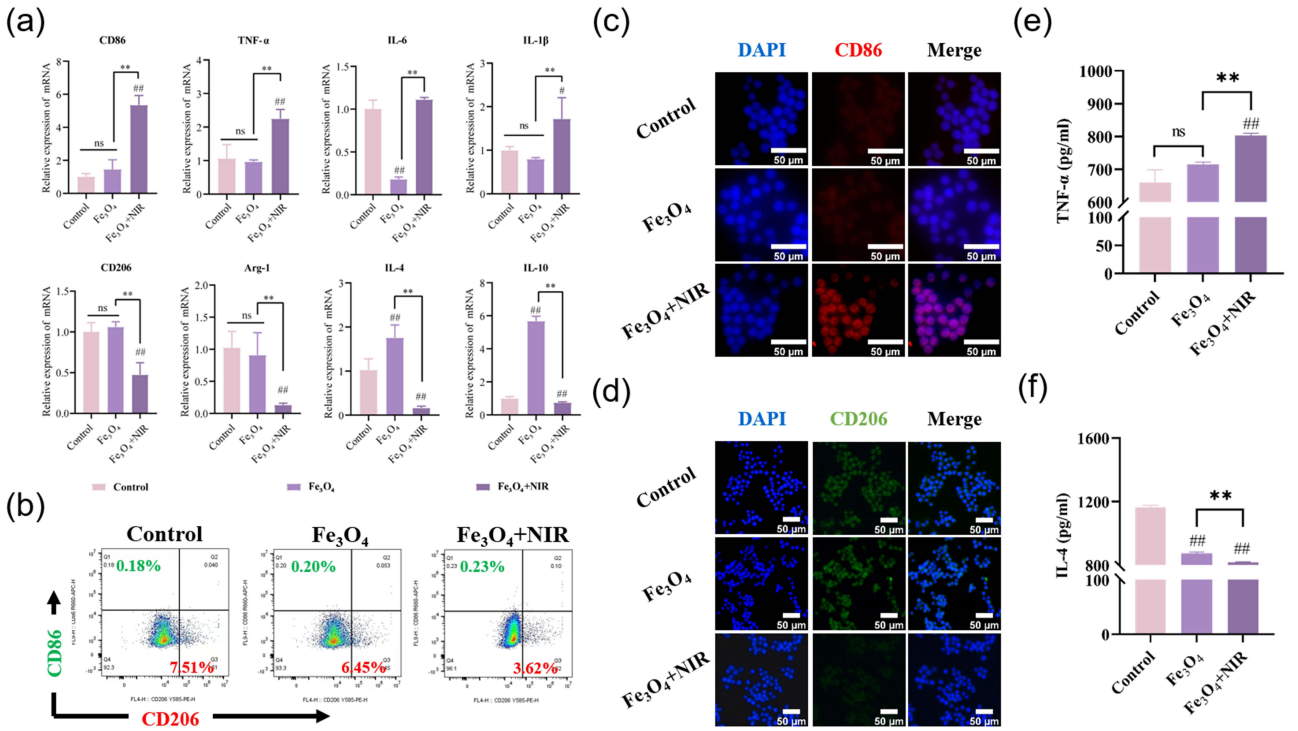


**Figure 3** Tumor-associated macrophage polarisation in vitro. (**a**) RAW264.7-related gene mRNA expression. (**b**) Flow cytometry detection of RAW264.7 macrophage polarisation. (**c**) CD86 immunofluorescence staining of RAW264.7 cells. (**d**) Immunofluorescence staining of RAW264.7 cells for CD206. (**e** and **f**) Elisa assay to detect TNF-α and IL-4 content in RAW264.7 cell supernatants. "#" indicates that the experimental group was statistically significant compared with the control group, $^{\#\#}p<0.01$. "*" means that the comparison between the two groups is statistically significant, $^{**}p<0.01$. The scale bar indicates 50 μm.

of oral squamous carcinoma cells through epidermal growth factor (EGF) stimulation and is associated with poor clinical prognosis in patients with oral squamous carcinoma.[59]

Tumor-promoting M2-polarised TAMs can promote angiogenesis, which induces tumor growth and metastasis.[60] M2 macrophages inhibit the immune system's anti-cancer effects by secreting the inhibitory factor IL-10, which suppresses the function of CD8+ T cells and NK cells, protects tumor cells from immune system-mediated recognition and cell death, and creates an immunosuppressive microenvironment in oral squamous cell carcinoma, in addition to enhancing the tumor's ability to escape the immune system.[61–64] Under photothermal action, $Fe_3O_4$ nanoparticles help tumor-associated macrophages become more polarised towards the M1 direction while decreasing the number of M2-type macrophages. This helps to stop tumor cell growth and enhance tumor immunity in vivo.

## $Fe_3O_4$ Photothermal Action Combined with PD-1/PD-L1 Inhibitors Anti-Tumor in vivo

We established the SCC7 animal model and treated mice in each group under different conditions 7 days after the local injection of tumor cells. We measured the temperature of the tumor site with a thermometer (Figure 4a). As shown in Figure 4b, the surface temperature of the animals in the control and immunotherapy groups without photothermal treatment was 36.8°C. The local temperatures of the NIR group and NIR+BMS-1 group reached 44°C and 43.1°C, respectively, after 808 nm NIR light irradiated the locally injected $Fe_3O_4$. This confirmed that $Fe_3O_4$ successfully played a photothermal role under the irradiation of NIR light. The impact of a combined therapeutic approach on tumor growth in vivo was evaluated by monitoring parameters such as tumor size (Figure 4c), tumor volume (Figure 4d), tumor weight (Figure 4e) and animal weight (Figure 4f).

As shown in Figure 4c and e, when comparing the tumor tissues in each group, the control group had the largest tumor size and weight, followed by the photothermal and immunosuppressive groups. In the combined photothermal and

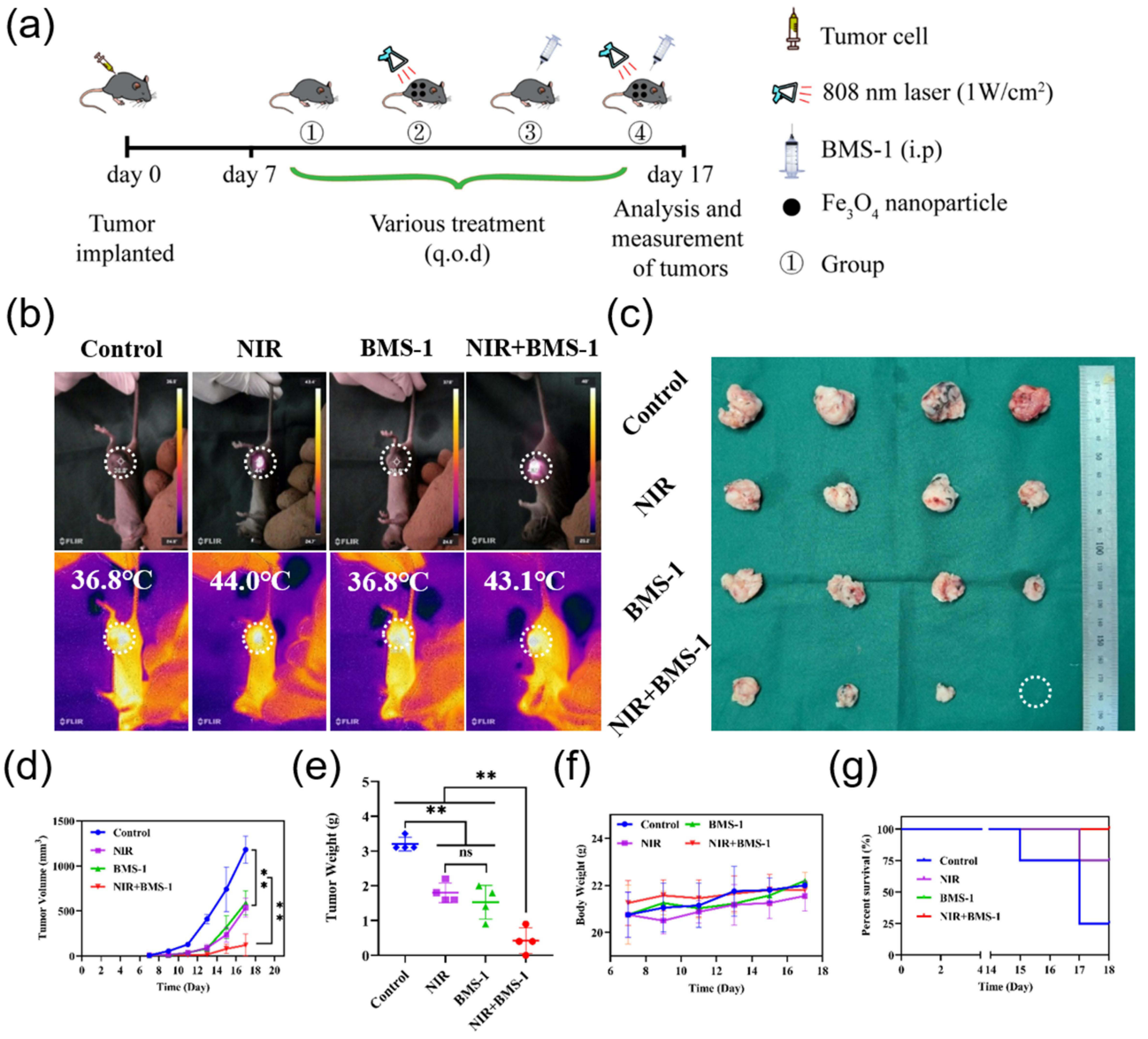


**Figure 4** In vivo anti-tumor effect of $Fe_3O_4$ photothermal action combined with PD1/PD-L1 inhibitor (BMS-1). (**a**) Schematic diagram of in vivo anti-tumor effect of SCC7 model. (**b**) Schematic diagram of tumor site temperature when tumors were treated under different conditions. (**c**) Primary tumors (n=4). (**d**) Primary tumor volume analysis (n=4). (**e**) Primary tumor body weight (n=4). (**f**) Mean body weight of mice (n=4). (**g**) Mouse survival analysis. "*" means that the comparison between the two groups is statistically significant, **p<0.01. The scale bar indicates 200 μm.

immunosuppression group, the tumor tissue was the smallest and lightest of the groups. This confirms that photothermal and immunosuppressive effects significantly inhibit tumor proliferation, and the combination can substantially impede tumor progression. As shown in the tumor volume analysis graph in Figure 4d, the tumor volume of the control group increased rapidly, and the importance of the NIR and BMS-1 groups rounded off slower than that of the control group. The tumor growth volume increase in the NIR+BMS-1 group was the lowest. Figure 4g shows the statistical graphs of the mice's survival analyses in each group. On the day of the experiment termination, the control group had a survival rate of only 25%, while the NIR and BMS-1 groups had a survival rate of 75%, and the NIR+BMS-1 group had a survival rate of 100%. The combination of photothermal action and immunosuppression in the mice's survival analysis prolonged their survival rate.

## Intra-Tumor Observations

The tumor tissues were stained to track changes in tumor development, necrosis, and apoptosis under various treatment methods, further confirming the synergistic effect of photothermal action and immunotherapy. As seen in Figure 5a, Prussian blue staining was used to examine the Fe elements in each group. The NIR photothermal therapy group and the NIR+BMS-1 photothermal therapy synergistic immunotherapy group both showed Prussian blue staining (black arrows), indicating the presence of Fe elements. The blank control and BMS-1 immunosuppressive treatment-only groups exhibited no Fe elements. The control group's tumors, when stained with H&E, were dense, morphologically intact cells. On the other hand, the other three groups saw loose tissue and cellular damage, particularly in the NIR+BMS-1 group that received photothermal therapy in addition to immunotherapy, which verified the presence of many dead cells.

ICD was initiated by releasing damage-associated molecular patterns (DAMPs) from dead cells, of which HMGB1 is the most critical. HMGB1 promotes the maturation of DCs, which activate cytotoxic T cells (CTLs). In the TME, HMGB1 released from damaged cancer cells induces ICD, which leads to CTL killing of cancer cells. In photothermia with immunosuppression, intracellular hyperthermia and immunosuppression cause the release of ICD and tumor-specific antigens, which activate CTLs.[32,65] This investigation confirmed the findings by identifying the immunohistochemistry expression of the ICD markers HMGB1 and HSP70. According to some research,

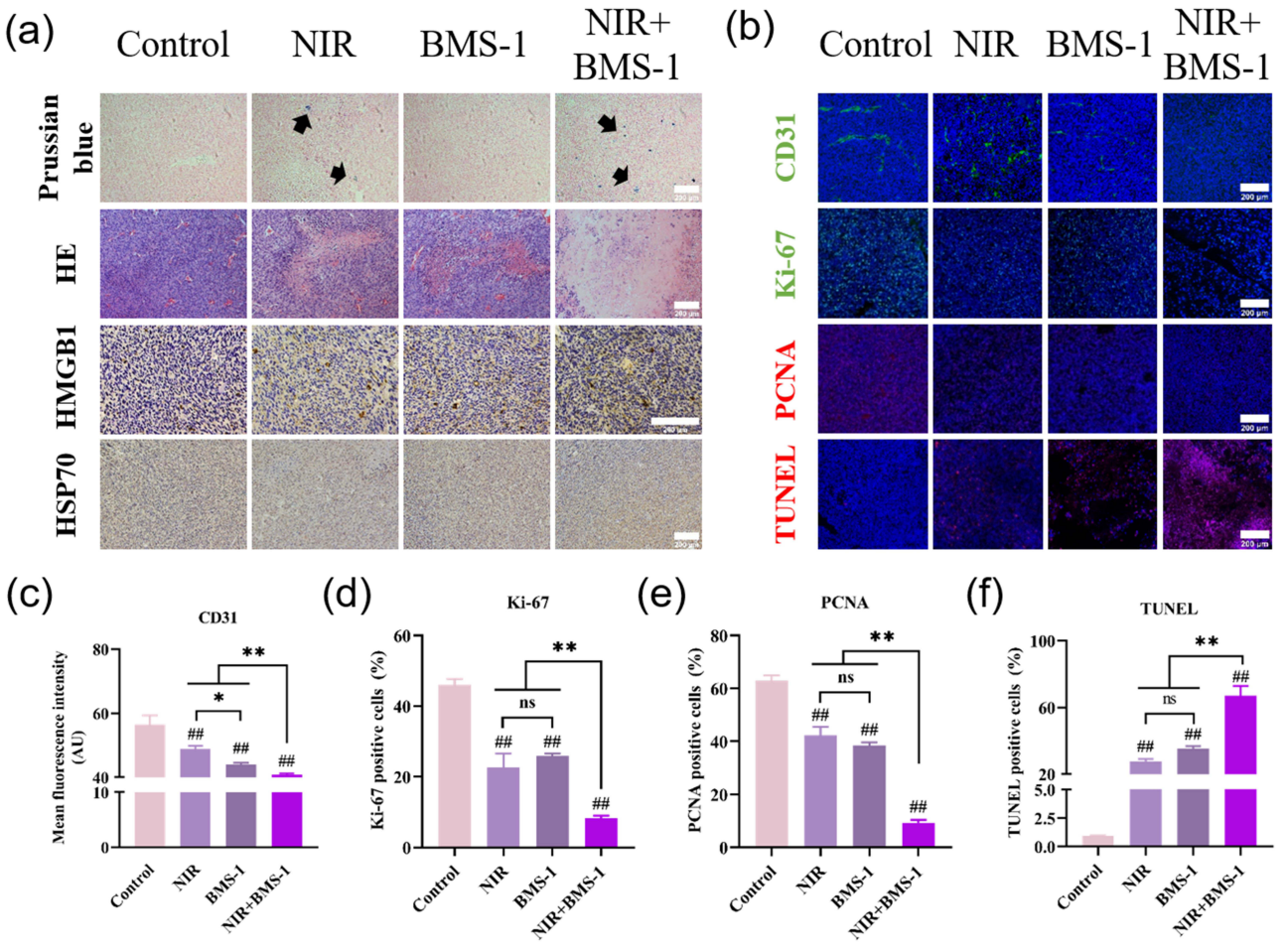


**Figure 5** In vivo staining of tumor tissue sections. (**a**) Prussian blue staining, HE staining, HMGB1 staining, HSP70 staining; (**b**) Immunofluorescence staining of tumor tissue for CD31 (green), Ki67 (green), PCNA (red), TUNEL (red). (**c**) Quantitative analysis of the average fluorescence intensity of CD31. (**d**) Quantification of Ki-67 positive cells from the fluorescence microscopy images of the tumor tissues. (**e**) Quantification of PCNA-positive cells from the fluorescence microscopy images of the tumor tissues. (**f**) Quantification of TUNEL-positive cells from the fluorescence microscopy images of the tumor tissues. "#" indicates that the experimental group was statistically significant compared with the control group, $^{\#\#}p<0.01$. "*" means that the comparison between the two groups is statistically significant, $^{*}p<0.05$,$^{**}p<0.01$. The scale bar indicates 200 μm.

inhibiting HSP60, HSP70, and other HSPs can make tumor cells less heat-resistant, more sensitive to PTT, and more effective at PTT.[24] It is reasonable that they assessed the relative amounts of HSP70 in these cells following PTT, as HSP70 improves heat resistance.[19] Figure 5a illustrates that the NIR+BMS-1 group had the highest expression of HMGB1 and HSP70 among the groups. This finding supports the hypothesis that photothermal action works with immunosuppression to induce ICD by stimulating the production of several heat shock proteins and facilitating the death of tumor cells by CTL.

The greenest fluorescent stain, CD31 (green) staining, was seen in the blank control group (Figure 5b), indicating the highest level of CD31 expression in the empty control group. The PTT synergistic immunotherapy group demonstrated the lowest expression of CD31, suggesting that the group's tumor reduction impact was amplified. We performed Figure 5c for CD31 expression in each group, and statistical analysis revealed that the control group had the highest mean fluorescence intensity, the NIR+BMS-1 group had the lowest, and fluorescence quantification was consistent with the staining trend.

By monitoring tumor tissues stained with Ki67 fluorescence, the impact of photothermal activity in conjunction with immunotherapy on the growth of tumor cells was evaluated. The control group exhibited the highest fluorescence, as seen in Figure 5b and d, and the statistical analysis's maximum percentage of Ki-67 positive cells was 46.1±1.3%. Conversely, the group that received photothermal action in addition to immunotherapy had a much lower rate of Ki-67 positive (8.3±0.6%), indicating that PTT synergistic immunotherapy effectively suppressed tumor cell growth.

In this investigation, PCNA immunofluorescence labeling was used to track tumor cell growth further. The control group, which did not receive any treatment intervention, had the highest tumor cell proliferation rate and red fluorescence emission, as demonstrated by PCNA staining in Figure 5b. Immunotherapy in conjunction with photothermal therapy resulted in the observation of slightly red PCNA fluorescence. Based on statistical analysis, the proportion of PCNA-positive cells in the control group was 62.9±1.7%, while in the photothermal treatment plus immunotherapy group, it was 9.3±0.9% (Figure 5e). The two results verified that PTT and immunotherapy synergistically suppressed tumor cell growth by following the same trend, which was in line with the findings of the Ki-67 staining.

TUNEL staining was used in this study to determine the number of apoptotic cells in the tumor tissues following treatment with various regimens. Figure 5b and f shows that the PTT synergistic immunotherapy group had the highest number of apoptotic cells, with a statistical analysis of 67.1±4.7%, while the control group had 0.9±0.1% versus CD31. It was established that, among the groups, PTT synergistic immunotherapy had the best tumor cell-killing efficacy. Through staining of the tumor tissue and statistical analysis, PTT synergistic immunotherapy was demonstrated to induce tumor necrosis and limit tumor proliferation successfully. PTT synergistic immunotherapy is a successful therapeutic approach for HNSCC, as observed through visualizing the tumor and molecular staining inside the tumor tissue.

## HE Staining of Animal Organs

The primary concern for implantable Materials is biosafety and research conducted in laboratory settings has demonstrated that a concentration of 2 mg/mL of $Fe_3O_4$ exhibits favorable biosafety properties. To further validate the in vivo safety, the present study was conducted by measuring the body weights of the animals every 2 days and observing the changes in the body weights of the animals, as shown in Figure 4f. There was no significant difference in the body weights of the animals in each group during the successive body weight measurements. In the meantime, this study further demonstrated the safety of $Fe_3O_4$ in vivo by observing the presence or absence of organic lesions in the mice's organs using HE staining. Figure 6 shows an observable absence of inflammatory reactions in the test subjects' hearts, livers, spleens, lungs, and kidneys within all experimental groups. This observation supports the idea that the synergistic impact of photothermal therapy and immunosuppression does not result in any negative consequences, thus presenting convincing evidence for its broad potential utility.

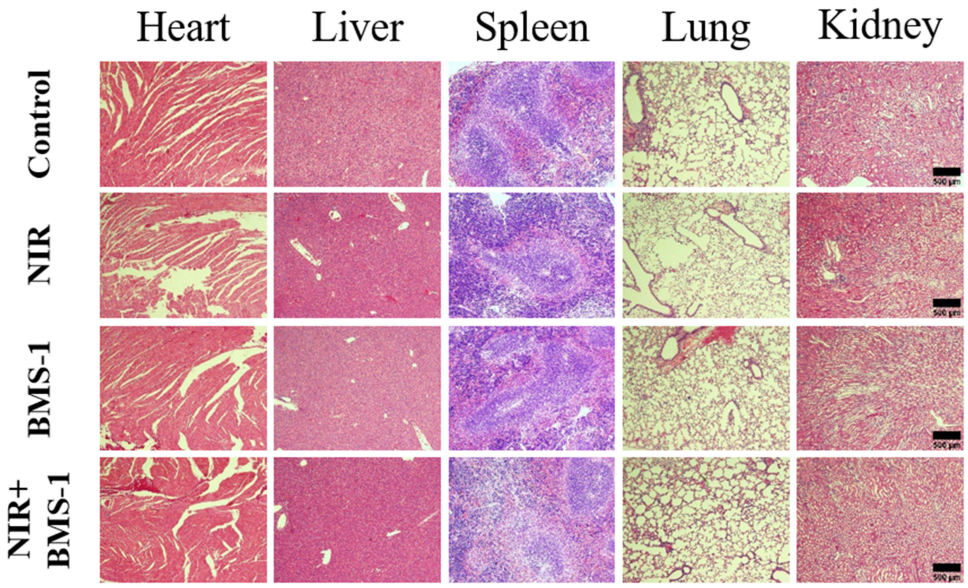


**Figure 6** HE staining analysis of major organs of four groups of mice after treatment. The scale bar indicates 500 μm.

## Conclusion

In this study, $Fe_3O_4$ nanoparticles were successfully synthesized, exhibiting favorable biocompatibility and a stable photothermal response. $Fe_3O_4$ photothermal not only can directly kill tumor cells and enhance the immunogenicity of the tumor microenvironment but also can regulate the polarization of tumor-associated macrophages and enhance the inhibitory effect on tumor cells. In in vitro experiments, combining photothermal action with immunotherapy, photothermal action kills tumor cells and improves the immunogenicity of the tumor microenvironment; PD-1/PD-L1 inhibitor reduces the immunosuppressive effect of the organism, which effectively achieves the inhibition of head and neck squamous carcinoma growth, significantly reduces the malignant proliferation of the tumor, and dramatically reduces the probability of tumor recurrence and distant metastasis. In Conclusion, combining photothermal therapy with immunotherapy provides a new, safe, and effective strategy for the treatment modality of oral cavity squamous carcinoma, which has a broad application prospect.

## Funding

This research was funded by the "Crossing" Research Fund Project of Ninth People's Hospital, affiliated to Shanghai Jiao Tong University School of Medicine (No. JYJC202102; No. JYJC202228), the Project of Shanghai Municipal Health and Family Planning Commission (No. 2019CXJQ01), the "Study on the Standardised and Large Scale Production and the Quality Assessment of Stem Cell Therapy Products (No. 2020YFA0112602)", and the "Funded by Peak Disciplines (Type IV) of Institutions of Higher Learning in Shanghai".

## Disclosure

The authors declare that they have no known competing financial interests or personal relationships that could have appeared to influence the work reported in this paper.

## References

1. Sato-Kaneko F, Yao S, Ahmadi A, et al. Combination immunotherapy with TLR agonists and checkpoint inhibitors suppresses head and neck cancer. *JCI Insight*. 2017;2(18). doi:10.1172/jci.insight.93397
2. Bu LL, Rao L, Yu GT, et al. Cancer stem cell-platelet hybrid membrane-coated magnetic nanoparticles for enhanced photothermal therapy of head and neck squamous cell carcinoma. *Adv. Funct. Mater.* 2019;29(10). doi:10.1002/adfm.201807733
3. Gupta B, Johnson NW, Kumar N. Global epidemiology of head and neck cancers: a continuing challenge. *Oncology*. 2016;91(1):13–23. doi:10.1159/000446117

4. Li S, Wang D, Cheng J, et al. A photodynamically sensitized dendritic cell vaccine that promotes the anti-tumor effects of anti-PD-L1 monoclonal antibody in a murine model of head and neck squamous cell carcinoma. *J Transl Med*. 2022;20(1):505. doi:10.1186/s12967-022-03707-x
5. Zhang X, Zhang L, Tan X, et al. Systematic analysis of genes involved in oral cancer metastasis to lymph nodes. *Cell Mol Biol Lett*. 2018;23(1):53. doi:10.1186/s11658-018-0120-2
6. Lin Y, Zhou J, Cheng Y, Zhao L, Yang Y, Wang J. Comparison of survival benefits of combined chemotherapy and radiotherapy versus chemotherapy alone for uterine serous carcinoma: a meta-analysis. *Int J Gynecol Cancer*. 2017;27(1):93–101. doi:10.1097/IGC.0000000000000856
7. Glasgow MD, Chougule MB. Recent developments in active tumor targeted multifunctional nanoparticles for combination chemotherapy in cancer treatment and imaging. *J Biomed Nanotechnol*. 2015;11(11):1859–1898. doi:10.1166/jbn.2015.2145
8. Huang X, Lu Y, Guo M, Du S, Han N. Recent strategies for nano-based PTT combined with immunotherapy: from a biomaterial point of view. *Theranostics*. 2021;11(15):7546–7569. doi:10.7150/thno.56482
9. Feng G, Fang Y, Liu J, et al. Multifunctional conjugated polymer nanoparticles for image-guided photodynamic and photothermal therapy. *Small*. 2017;13(3). doi:10.1002/smll.201602807
10. Sun Q, You Q, Pang X, et al. A photoresponsive and rod-shape nanocarrier: single wavelength of light triggered photothermal and photodynamic therapy based on AuNRs-capped & Ce6-doped mesoporous silica nanorods. *Biomaterials*. 2017;122:188–200. doi:10.1016/j.biomaterials.2017.01.021
11. Huang L, Li Y, Du Y, et al. Mild photothermal therapy potentiates anti-PD-L1 treatment for immunologically cold tumors via an all-in-one and all-in-control strategy. *Nat Commun*. 2019;10(1):4871. doi:10.1038/s41467-019-12771-9
12. Liu XZ, Wen ZJ, Li YM, et al. Bioengineered bacterial membrane vesicles with multifunctional nanoparticles as a versatile platform for cancer immunotherapy. *ACS Appl Mater Interfaces*. 2023;15(3):3744–3759. doi:10.1021/acsami.2c18244
13. Zhao N, Yan L, Xue J, Zhang K, Xu F-J. Degradable one-dimensional dextran-iron oxide nanohybrids for MRI-guided synergistic gene/photothermal/magnetolytic therapy. *Nano Today*. 2021;38. doi:10.1016/j.nantod.2021.101118
14. Ge R, Liu C, Zhang X, et al. Photothermal-activatable Fe(3)O(4) superparticle nanodrug carriers with PD-L1 immune checkpoint blockade for anti-metastatic cancer immunotherapy. *ACS Appl Mater Interfaces*. 2018;10(24):20342–20355. doi:10.1021/acsami.8b05876
15. Lan P, Chen H, Guo Y, et al. NIR-II responsive molybdenum dioxide nanosystem manipulating cellular immunogenicity for enhanced tumor photoimmunotherapy. *Nano Lett*. 2022;22(12):4741–4749. doi:10.1021/acs.nanolett.2c00899
16. He S, Li J, Cheng P, et al. Charge-reversal polymer nano-modulators for photodynamic immunotherapy of cancer. *Angew Chem Int Ed Engl*. 2021;60(35):19355–19363. doi:10.1002/anie.202106392
17. Serrano-Del Valle A, Naval J, Anel A, Marzo I. Novel forms of immunomodulation for cancer therapy. *Trends Cancer*. 2020;6(6):518–532. doi:10.1016/j.trecan.2020.02.015
18. Duan X, Chan C, Lin W. Nanoparticle-mediated immunogenic cell death enables and potentiates cancer immunotherapy. *Angew Chem Int Ed Engl*. 2019;58(3):670–680. doi:10.1002/anie.201804882
19. Xu P, Liang F. Nanomaterial-based tumor photothermal immunotherapy. *Int J Nanomed*. 2020;15:9159–9180. doi:10.2147/IJN.S249252
20. Alamzadeh Z, Beik J, Pirhajati Mahabadi V, et al. Ultrastructural and optical characteristics of cancer cells treated by a nanotechnology based chemo-photothermal therapy method. *J Photochem Photobiol B*. 2019;192:19–25. doi:10.1016/j.jphotobiol.2019.01.005
21. Mocan T, Matea CT, Cojocaru I, et al. Photothermal treatment of human pancreatic cancer using PEGylated multi-walled carbon nanotubes induces apoptosis by triggering mitochondrial membrane depolarization mechanism. *J Cancer*. 2014;5(8):679–688. doi:10.7150/jca.9481
22. Ali MR, Wu Y, Han T, et al. Simultaneous time-dependent surface-enhanced raman spectroscopy, metabolomics, and proteomics reveal cancer cell death mechanisms associated with gold nanorod photothermal therapy. *J Am Chem Soc*. 2016;138(47):15434–15442. doi:10.1021/jacs.6b08787
23. van den Tempel N, Horsman MR, Kanaar R. Improving efficacy of hyperthermia in oncology by exploiting biological mechanisms. *Int J Hyperthermia*. 2016;32(4):446–454. doi:10.3109/02656736.2016.1157216
24. Wang Z, Li S, Zhang M, et al. Laser-triggered small interfering RNA releasing gold nanoshells against heat shock protein for sensitized photothermal therapy. *Adv Sci*. 2017;4(2):1600327. doi:10.1002/advs.201600327
25. Ali MR, Ali HR, Rankin CR, El-Sayed MA. Targeting heat shock protein 70 using gold nanorods enhances cancer cell apoptosis in low dose plasmonic photothermal therapy. *Biomaterials*. 2016;102:1–8. doi:10.1016/j.biomaterials.2016.06.017
26. Galluzzi L, Buque A, Kepp O, Zitvogel L, Kroemer G. Immunogenic cell death in cancer and infectious disease. *Nat Rev Immunol*. 2017;17(2):97–111. doi:10.1038/nri.2016.107
27. Chen Q, Hu Q, Dukhovlinova E, et al. Photothermal therapy promotes tumor infiltration and antitumor activity of CAR T cells. *Adv Mater*. 2019;31(23):e1900192. doi:10.1002/adma.201900192
28. Jiang Y, Huang J, Xu C, Pu K. Activatable polymer nanoagonist for second near-infrared photothermal immunotherapy of cancer. *Nat Commun*. 2021;12(1):742. doi:10.1038/s41467-021-21047-0
29. Huang J, Zhang L, Zhou W, et al. Dual mitigation of immunosuppression combined with photothermal inhibition for highly effective primary tumor and metastases therapy. *Biomaterials*. 2021;274:120856. doi:10.1016/j.biomaterials.2021.120856
30. Liu P, Peng Y, Zhou Y, et al. Rapamycin as a "One-Stone-Three-Birds" agent for cooperatively enhanced phototherapies against metastatic breast cancer. *ACS Appl Mater Interfaces*. 2021;13(22):25674–25684. doi:10.1021/acsami.1c03312
31. Zhang C, Zeng Z, Cui D, He S, Jiang Y. Semiconducting polymer nano-PROTACs for activatable photo-immunometabolic cancer therapy. *Nat Commun*. 2021;12(1):2934. doi:10.1038/s41467-021-23194-w
32. Liu X, Feng Y, Xu J, et al. Combination of MAPK inhibition with photothermal therapy synergistically augments the anti-tumor efficacy of immune checkpoint blockade. *J Control Release*. 2021;332:194–209. doi:10.1016/j.jconrel.2021.02.020
33. Yata T, Takahashi Y, Tan M, et al. DNA nanotechnology-based composite-type gold nanoparticle-immunostimulatory DNA hydrogel for tumor photothermal immunotherapy. *Biomaterials*. 2017;146:136–145. doi:10.1016/j.biomaterials.2017.09.014
34. Moy AJ, Tunnell JW. Combinatorial immunotherapy and nanoparticle mediated hyperthermia. *Adv Drug Deliv Rev*. 2017;114:175–183. doi:10.1016/j.addr.2017.06.008
35. Li Y, He L, Dong H, et al. Fever-inspired immunotherapy based on photothermal CpG nanotherapeutics: the critical role of mild heat in regulating tumor microenvironment. *Adv Sci*. 2018;5(6):1700805. doi:10.1002/advs.201700805
36. Deng X, Shao Z, Zhao Y. Solutions to the drawbacks of photothermal and photodynamic cancer therapy. *Adv Sci*. 2021;8(3):2002504. doi:10.1002/advs.202002504

37. Riley RS, Day ES. Gold nanoparticle-mediated photothermal therapy: applications and opportunities for multimodal cancer treatment. *Wiley Interdiscip Rev Nanomed Nanobiotechnol*. 2017;9(4). doi:10.1002/wnan.1449
38. Ng CW, Li J, Pu K. Recent progresses in phototherapy-synergized cancer immunotherapy. *Adv Funct Mater*. 2018;28(46):3.
39. Feng M, Xiong G, Cao Z, et al. PD-1/PD-L1 and immunotherapy for pancreatic cancer. *Cancer Lett*. 2017;407:57–65. doi:10.1016/j.canlet.2017.08.006
40. Shen X, Zhao B. Efficacy of PD-1 or PD-L1 inhibitors and PD-L1 expression status in cancer: meta-analysis. *BMJ*. 2018;362:k3529. doi:10.1136/bmj.k3529
41. Bauml J, Seiwert TY, Pfister DG, et al. Pembrolizumab for platinum- and cetuximab-refractory head and neck cancer: results from a single-arm, Phase II study. *J Clin Oncol*. 2017;35(14):1542–1549. doi:10.1200/JCO.2016.70.1524
42. Tahara M, Muro K, Hasegawa Y, et al. Pembrolizumab in Asia-Pacific patients with advanced head and neck squamous cell carcinoma: analyses from KEYNOTE-012. *Cancer Sci*. 2018;109(3):771–776. doi:10.1111/cas.13480
43. Shao K, Singha S, Clemente-Casares X, Tsai S, Yang Y, Santamaria P. Nanoparticle-based immunotherapy for cancer. *ACS Nano*. 2015;9(1):16–30. doi:10.1021/nn5062029
44. Li X, Lovell JF, Yoon J, Chen X. Clinical development and potential of photothermal and photodynamic therapies for cancer. *Nat Rev Clin Oncol*. 2020;17(11):657–674. doi:10.1038/s41571-020-0410-2
45. Wang X, Qi Y, Hu Z, et al. Fe3O4@PVP@DOX magnetic vortex hybrid nanostructures with magnetic-responsive heating and controlled drug delivery functions for precise medicine of cancers. *Adv Compos Hybrid Mater*. 2022;5(3):1786–1798. doi:10.1007/s42114-022-00433-2
46. Li Y, Hu D, Pan M, et al. Near-infrared light and redox dual-activatable nanosystems for synergistically cascaded cancer phototherapy with reduced skin photosensitization. *Biomaterials*. 2022;288:121700. doi:10.1016/j.biomaterials.2022.121700
47. Zhu P, Jin Z, Kang G, et al. Alpha5 nicotinic acetylcholine receptor mediated immune escape of lung adenocarcinoma via STAT3/Jab1-PD-L1 signalling. *Cell Commun Signal*. 2022;20(1):121. doi:10.1186/s12964-022-00934-z
48. Guo X, Wu Z, Li W, et al. Appropriate size of magnetic nanoparticles for various bioapplications in cancer diagnostics and therapy. *ACS Appl Mater Interfaces*. 2016;8(5):3092–3106. doi:10.1021/acsami.5b10352
49. Albanese A, Tang PS, Chan WC. The effect of nanoparticle size, shape, and surface chemistry on biological systems. *Annu Rev Biomed Eng*. 2012;14(1):1–16. doi:10.1146/annurev-bioeng-071811-150124
50. Shen S, Wang S, Zheng R, et al. Magnetic nanoparticle clusters for photothermal therapy with near-infrared irradiation. *Biomaterials*. 2015;39:67–74. doi:10.1016/j.biomaterials.2014.10.064
51. Zhu M, Nie G, Meng H, Xia T, Nel A, Zhao Y. Physicochemical properties determine nanomaterial cellular uptake, transport, and fate. *Acc Chem Res*. 2013;46(3):622–631. doi:10.1021/ar300031y
52. Nel A, Xia T, Meng H, et al. Nanomaterial toxicity testing in the 21st century: use of a predictive toxicological approach and high-throughput screening. *Acc Chem Res*. 2013;46(3):607–621. doi:10.1021/ar300022h
53. Zhang F, Parayath NN, Ene CI, et al. Genetic programming of macrophages to perform anti-tumor functions using targeted mRNA nanocarriers. *Nat Commun*. 2019;10(1):3974. doi:10.1038/s41467-019-11911-5
54. Boutilier AJ, Elsawa SF. Macrophage polarization states in the tumor microenvironment. *Int J Mol Sci*. 2021;22(13):6995. doi:10.3390/ijms22136995
55. Umemura N, Sugimoto M, Kitoh Y, Saio M, Sakagami H. Metabolomic profiling of tumor-infiltrating macrophages during tumor growth. *Cancer Immunol Immunother*. 2020;69(11):2357–2369. doi:10.1007/s00262-020-02622-8
56. Guo L, Yan DD, Yang D, et al. Combinatorial photothermal and immuno cancer therapy using chitosan-coated hollow copper sulfide nanoparticles. *ACS Nano*. 2014;8(6):5670–5681. doi:10.1021/nn5002112
57. Li L, Yang S, Song L, et al. An endogenous vaccine based on fluorophores and multivalent immunoadjuvants regulates tumor micro-environment for synergistic photothermal and immunotherapy. *Theranostics*. 2018;8(3):860–873. doi:10.7150/thno.19826
58. Chen Y, Song Y, Du W, Gong L, Chang H, Zou Z. Tumor-associated macrophages: an accomplice in solid tumor progression. *J Biomed Sci*. 2019;26(1):78. doi:10.1186/s12929-019-0568-z
59. Haque A, Moriyama M, Kubota K, et al. CD206(+) tumor-associated macrophages promote proliferation and invasion in oral squamous cell carcinoma via EGF production. *Sci Rep*. 2019;9(1):14611. doi:10.1038/s41598-019-51149-1
60. Hourani T, Holden JA, Li W, Lenzo JC, Hadjigol S, O'Brien-Simpson NM. Tumor associated macrophages: origin, recruitment, phenotypic diversity, and targeting. *Front Oncol*. 2021;11:788365. doi:10.3389/fonc.2021.788365
61. Mori K, Hiroi M, Shimada J, Ohmori Y. Infiltration of m2 tumor-associated macrophages in oral squamous cell carcinoma correlates with tumor malignancy. *Cancers*. 2011;3(4):3726–3739. doi:10.3390/cancers3043726
62. Ostuni R, Kratochvill F, Murray PJ, Natoli G. Macrophages and cancer: from mechanisms to therapeutic implications. *Trends Immunol*. 2015;36(4):229–239. doi:10.1016/j.it.2015.02.004
63. Xue Y, Song X, Fan S, Deng R. The role of tumor-associated macrophages in oral squamous cell carcinoma. *Front Physiol*. 2022;13:959747. doi:10.3389/fphys.2022.959747
64. Kubota K, Moriyama M, Furukawa S, et al. CD163(+)CD204(+) tumor-associated macrophages contribute to T cell regulation via interleukin-10 and PD-L1 production in oral squamous cell carcinoma. *Sci Rep*. 2017;7(1):1755. doi:10.1038/s41598-017-01661-z
65. Li X, Zheng J, Chen S, Meng FD, Ning J, Sun SL. Oleandrin, a cardiac glycoside, induces immunogenic cell death via the PERK/elF2alpha/ATF4/CHOP pathway in breast cancer. *Cell Death Dis*. 2021;12(4):314. doi:10.1038/s41419-021-03605-y